Phase-field study on the effects of process and material parameters on the tilt angle during directional solidification of ternary eutectics

CrossMark

Kaveh Dargahi Noubary [a,*,1], Michael Kellner [a,b,1], Philipp Steinmetz [a,1], Johannes Hötzer [a,b,1], Britta Nestler [a,b]

[a] *Institute of Applied Materials, Karlsruhe Institute of Technology (KIT), Straße am Forum 7, 76131 Karlsruhe, Germany*
[b] *Institute of Materials and Processes, Karlsruhe University of Applied Sciences, Moltkestrasse 30, 76133 Karlsruhe, Germany*

ABSTRACT

In the directional solidification of molten alloys, the configuration of growing phases plays a vital role in the properties of the resulting materials. During directional eutectic solidification, the growth direction and the velocity can be controlled by an imprinted temperature gradient. For this kind of process, different instabilities can occur. One observed instability is tilted growth of the solid phases against the direction of the imprinted temperature gradient. In ternary eutectics this phenomenon can occur in systems with isotropic phases. To investigate the effects of the different process and material parameters, simulation studies with a thermodynamically consistent phase-field model based on the grand potential approach, are conducted. An idealized system with different isotropic interfacial energies, diffusion coefficients, lamellar spacings, solidification velocities and slopes of the imposed temperature gradient is systematically studied. The effects on tilting are analyzed and discussed. To quantitatively determine the tilt angle automatized, an unsupervised measurement method is developed. Based on the results of the measurements, a fitting function is derived to predict the tilt angles.

© 2017 Elsevier B.V. All rights reserved.

1. Introduction

The improvement of material properties is crucial for different technical applications [1]. The final microstructure influences the macroscopic material properties [2], like its mechanical, electrical, optical, acoustic, tribological, thermal and magnetic properties. Scientific investigations of the influence of the melt composition and of the process parameters on the evolving microstructure have improved the materials and the understanding of solidification in the last decades.

Besides experiments and analytic approaches, simulation methods have been established in recent years, to study the microstructure evolution during solidification. Especially the possibility to study the effect of different physical parameter and process parameters in complex spatial arrangements using the phase-field method allows to gain new insights into the solidification process [1,3]. During diffusion controlled directional solidification of a eutectic composition, different phases evolve in a coupled manner and form various arrangements in the microstructure [4]. In eutectic alloys different instabilities in the microstructure, such as bifurcation [5,6], growth of eutectic

colonies [7,3,8,9], oscillations in the phase widths [5,10–13] and tilting in sections perpendicular to the growth direction [15,14,16–18], can be observed. In the case of tilting, the phases evolve with a deviation between the solid-solid interfaces and the direction of the imprinted temperature gradient. This leads to an undefined direction of the evolving phases and hence to different macroscopic material properties. Therefore, it is important to gain a better insight into the fundamental principles of tilted growth.

The two dimensional phenomenon of tilted growth for binary systems is investigated experimentally in [14,16], theoretically in [17] and numerically with phase-field simulations in [16,18–20]. It is found that tilted growth in binary eutectics is a result of anisotropic interface energies. Further, it is observed that the tilt angle does increase when the lamellar spacing is increased [9,13,14,21,22]. However Ghosh et al. do not confirm this behavior in [18,19] with their phase-field simulations and dynamic boundary integral studies. For these investigations, slow growth velocities and small Péclet numbers are used in the vicinity of the lamellar spacing with the minimum undercooling. In [9], Akamatsu et al. illustrate the dependence of the tilt angle on the lamellar spacing with a second order polynomial fit.

In multicomponent multiphase systems further effects besides anisotropy can cause tilted growth. For phase-field simulations of ternary eutectics, tilting is reported for crystallographic isotropic

---

* Corresponding author.
  E-mail address: kaveh.noubary@kit.edu (K. Dargahi Noubary).
[1] The authors contributed equally.

systems [23,24]. Apel et al. [23] describe the behavior of tilting for an asymmetric ternary phase diagram with a three phase sequence of $\alpha\beta\delta$. In contrast to the observed modes in binary alloys, tilted growth is a result of the lack of mirror symmetries in the diffusion field of the ternary system. Tilted growth due to different but isotropic interface energies is investigated for various parameters by Hötzer et al. [24]. By varying the ratio of the interface energies between the solid phases α and β and the interface energies of the solid-liquid phase boundaries ($\alpha\ell$), tilting can be observed.

Further, the phase equilibria can influence the tilt angle experimentally and in phase-field simulations, as shown for the ternary system $CBr_4 - C_2Cl_6$ [22]. For this system, tilting occurs as a response of different growth velocities [25], demonstrating the influence of the process conditions on the tilt angle.

To improve the understanding of the mechanisms that influence the tilt angle during the directional solidification of ternary eutectics, different physical parameters and process parameters are systematically varied in this work. For this purpose, extensive studies of 2D phase-field simulations are conducted, and the resulting tilt angles are measured with an unsupervised and automatized method. First, the applied model and simulation setup is introduced, and a quantitative method is given to measure the tilt angle. The effects of different lamellar spacings, diffusion coefficients, interface energy ratios, temperature gradients and growth velocities on the resulting tilt angle are analyzed. Based on these results, a general fitting approach is then derived to predict the tilt angle depending on the investigated parameters.

2. Methods

In this section the applied phase-field model is introduced, the setup for the simulations is illustrated and the variation ranges of the analyzed parameters are explained. Further, the method for measuring the resulting tilt angles in the simulations is described.

2.1. Phase-field model

To investigate tilted growth, the phase-field model based on the thermodynamic grand potential approach is derived in [26,27] and is presented in [28]. The model is spatially discretized with a finite difference scheme and the temporal evolution is calculated by an explicit Euler scheme, as described e.g. in [29]. The implementation of the model into the massive parallel framework waLBerla[2] [30] and the used optimizations are presented in [28,31,32]. Quantitative investigations of different aspects of directional solidification of ternary alloys with the applied model are shown in [24,28,33–38].

For the simulation of directional solidification, the coupled set of partial differential equations of the form

$$\frac{\partial T}{\partial t} = \frac{\partial}{\partial t}(T_0 + G(z - vt)) = -Gv \tag{3}$$

are solved. The evolution Eqs. (1) for the $N = 4$ phase-fields $\phi_{\hat{\alpha}}$ are derived with an Allen-Cahn type approach from the grand potential functional. The Lagrange multiplier Λ is utilized to fulfill the constraint $\sum_{\hat{\alpha}=1}^{N}\partial\phi_{\hat{\alpha}}/\partial t = 0$ and $\hat{\alpha}, \hat{\beta}$ and $\hat{\gamma}$ represent phase indices. To calculate the driving force for the phase transition, the grand potentials $\psi_{\hat{\alpha}}$ of the system are determined. While the kinetics of the diffuse interface is described by the parameter τ, its thickness is related to the parameter ϵ. The diffuse interface is modeled with the gradient energy density a, given as

$$a(\boldsymbol{\phi}, \nabla\boldsymbol{\phi}) = \sum_{\hat{\alpha}<\hat{\beta}}^{N,N}\gamma_{\hat{\alpha}\hat{\beta}}|q_{\hat{\alpha}\hat{\beta}}|^2 \tag{4}$$

and the potential energy ω is expressed as an obstacle-type potential energy by

$$\omega(\boldsymbol{\phi}) = \frac{16}{\pi^2}\sum_{\hat{\alpha}<\hat{\beta}}^{N,N}\gamma_{\hat{\alpha}\hat{\beta}}\phi_{\hat{\alpha}}\phi_{\hat{\beta}} + \sum_{\hat{\alpha}<\hat{\beta}<\hat{\delta}}^{N,N,N}\gamma_{\hat{\alpha}\hat{\beta}\hat{\delta}}\phi_{\hat{\alpha}}\phi_{\hat{\beta}}\phi_{\hat{\delta}}. \tag{5}$$

Both a and ω depend on the isotropic interface energies $\gamma_{\hat{\alpha}\hat{\beta}}$. The parameter $\gamma_{\hat{\alpha}\hat{\beta}\hat{\delta}}$ is introduced to suppress the occurrence of third or higher order phases in binary interfaces [39,29].

Based on the assumption of mass conservation and on Fick's laws, the evolution Eqs. (2) for the $K = 3$ chemical potentials $\boldsymbol{\mu}$ are derived. The interpolation function $h_{\hat{\alpha}}(\boldsymbol{\phi})$ is used to scale the values in the diffuse interface.

To balance the effects of the artificially enlarged interface, an anti-trapping current, $\boldsymbol{J}_{at}$, is introduced [27,40,41]. The mobilities of the chemical potentials $\boldsymbol{\mu}$ are given by the matrix $\boldsymbol{M}$, which is described as

$$\boldsymbol{M}(\boldsymbol{\phi}, \boldsymbol{\mu}, T) = \sum_{\hat{\alpha}=1}^{N}\boldsymbol{D}_{\hat{\alpha}}\frac{\partial\boldsymbol{c}_{\hat{\alpha}}(\boldsymbol{\mu}, T)}{\partial\boldsymbol{\mu}}h_{\hat{\alpha}}(\boldsymbol{\phi}) \tag{6}$$

with the diffusion matrix $\boldsymbol{D}_{\hat{\alpha}}$. The concentration vector $\boldsymbol{c}_{\hat{\alpha}}(\boldsymbol{\mu}, T)$ contains the values of the K chemical elements in the corresponding phase $\hat{\alpha}$. As presented in [42], the derivative $\partial\boldsymbol{c}_{\hat{\alpha}}/\partial\boldsymbol{\mu}$ is calculated from the parabolic Gibbs energies.

The evolution of the analytic temperature field, depending on the base temperature T_0 and on the applied gradient G, with the velocity v in the growth direction z, is described by Eq. (3). The approximation of the temperature by means of an analytical approach relies on the assumption that heat diffusion is multiple times faster than mass diffusion, resulting in a significant reduction of the computational effort.

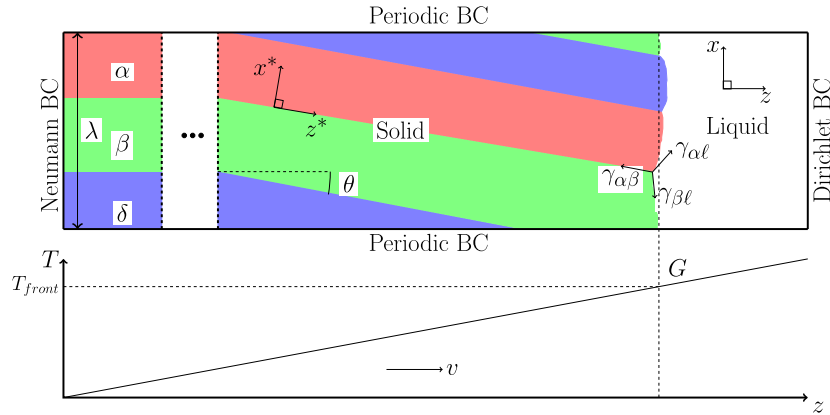$$\tau\epsilon\frac{\partial\phi_{\hat{\alpha}}}{\partial t} = \underbrace{-\epsilon T\left(\frac{\partial a(\boldsymbol{\phi}, \nabla\boldsymbol{\phi})}{\partial\phi_{\hat{\alpha}}} - \nabla\cdot\frac{\partial a(\boldsymbol{\phi}, \nabla\boldsymbol{\phi})}{\partial\nabla\phi_{\hat{\alpha}}}\right) - \frac{T}{\epsilon}\frac{\partial\omega(\boldsymbol{\phi})}{\partial\phi_{\hat{\alpha}}}}_{\text{interface contribution}} \underbrace{- \frac{\partial\psi(\boldsymbol{\phi}, \boldsymbol{\mu}, T)}{\partial\phi_{\hat{\alpha}}}}_{\text{bulk contribution}} + \underbrace{\frac{1}{N}\sum_{\hat{\beta}=1}^{N}rhs_{\hat{\beta}}}_{\Lambda}, \tag{1}$$

$$\underbrace{\qquad\qquad\qquad\qquad\qquad\qquad\qquad\qquad}_{:=rhs_{\hat{\alpha}}}$$

$$\frac{\partial\boldsymbol{\mu}}{\partial t} = \left[\sum_{\hat{\alpha}=1}^{N}h_{\hat{\alpha}}(\boldsymbol{\phi})\left(\frac{\partial\boldsymbol{c}_{\hat{\alpha}}(\boldsymbol{\mu}, T)}{\partial\boldsymbol{\mu}}\right)\right]^{-1} - \left(\nabla\cdot\left(\boldsymbol{M}(\boldsymbol{\phi}, \boldsymbol{\mu}, T)\nabla\boldsymbol{\mu} - \boldsymbol{J}_{at}(\boldsymbol{\phi}, \boldsymbol{\mu}, T) - \sum_{\hat{\alpha}=1}^{N}\boldsymbol{c}_{\hat{\alpha}}(\boldsymbol{\mu}, T)\frac{\partial h_{\hat{\alpha}}(\boldsymbol{\phi})}{\partial t} - \sum_{\hat{\alpha}=1}^{N}h_{\hat{\alpha}}(\boldsymbol{\phi})\left(\frac{\partial\boldsymbol{c}_{\hat{\alpha}}(\boldsymbol{\mu}, T)}{\partial T}\right)\frac{\partial T}{\partial t}\right), \tag{2}$$

Fig. 1. Simulation setup of the three solid phases α, β and δ to investigate tilted growth. For the domain a temperature gradient profile is applied and the indicated boundary conditions (BCs) are constructed at the domain boundaries.

Table 1
Summary of the physical parameters related to a symmetric ternary eutectic phase diagram with equal phase fractions from [24]. The Gibbs energies of the solid phases are modeled with the parameters $\Xi_{\hat{\alpha}}, \xi_{\hat{\alpha}}, X_{\hat{\alpha}}$ as congruent paraboloids, symmetrically distributed around the liquid paraboloid which is located in the center of the simplex. The varied values for $\gamma_{\alpha\beta}$ and $\gamma_{\alpha\ell}$ are given in eftab:parameters.

parameter	simulation value
γ	$\begin{array}{c c} & \begin{array}{cccc} \text{phase} & \alpha & \beta & \delta & \ell \end{array} \\ \begin{array}{c} \alpha \\ \beta \\ \delta \\ \ell \end{array} & \begin{bmatrix} - & \gamma_{\alpha\beta} & 0.2 & \gamma_{\alpha\ell} \\ \gamma_{\alpha\beta} & - & 0.2 & 0.2 \\ 0.2 & 0.2 & - & 0.2 \\ \gamma_{\alpha\ell} & 0.2 & 0.2 & - \end{bmatrix} \end{array}$
$\boldsymbol{c}_\ell = \left[c_A^\ell, c_B^\ell, c_C^\ell \right]$	$0.\bar{3}, 0.\bar{3}, 0.\bar{3}$ mol-%
$\Xi_{\hat{\alpha}}, \boldsymbol{\xi}_{\hat{\alpha}}, X_{\hat{\alpha}}$	$\begin{bmatrix} 2 & 1 \\ 1 & 2 \end{bmatrix}, \begin{bmatrix} -2.8 \\ -2.0 \end{bmatrix}, 1.04$
$\Xi_{\beta}, \boldsymbol{\xi}_{\beta}, X_{\beta}$	$\begin{bmatrix} 2 & 1 \\ 1 & 2 \end{bmatrix}, \begin{bmatrix} -2.0 \\ -2.8 \end{bmatrix}, 1.04$
$\Xi_{\delta}, \boldsymbol{\xi}_{\delta}, X_{\delta}$	$\begin{bmatrix} 2 & 1 \\ 1 & 2 \end{bmatrix}, \begin{bmatrix} -1.2 \\ -1.2 \end{bmatrix}, 0.24$
$\Xi_{\ell}, \boldsymbol{\xi}_{\ell}, X_{\ell}$	$\begin{bmatrix} 2 & 1 \\ 1 & 2 \end{bmatrix}, \begin{bmatrix} -2.0 \\ -2.0 \end{bmatrix}, 3.\bar{3} - 2.\bar{6}T$
$T_{eutectic}$	1.0
phase fraction of α, β, γ	$0.\bar{3}, 0.\bar{3}, 0.\bar{3}$
$\gamma_{\alpha\beta\delta}$	2.6

2.2. Setup

To investigate the tilt angle dependence on the physical parameters and on the process parameters, a defined initial phase arrangement is applied for all simulations. Starting from a lamellar arrangement of an $\alpha\beta\delta$ stacking sequence (similar to [23]) with solid-solid phase boundaries parallel to the growth direction as shown in the left part of Fig. 1, the three solid phases of the ternary eutectic alloy grow into the liquid. The growth is driven by the imposed analytical temperature gradient. The width of the periodic

lamellar arrangement perpendicular to the imprinted temperature direction is defined as λ. During the growth a front temperature T_{front} adjusts at the interface, which is slightly below the ternary eutectic temperature T_E.

On the left side of the domain with the three solid phases in Fig. 1, a Neumann boundary condition is utilized. On the opposite side, a Dirichlet condition is applied to model an infinite liquid domain ahead of the growth front. Perpendicular to the solidification direction, periodicity for both phase-fields and chemical potentials is used to simulate an infinitely large solidification front.

Table 2
Summary of the variations in the interface energy ratios r_1) to r_3), the diffusion coefficients d_1) to d_3), the temperature gradient t_1) to t_3), its imprinted velocity v_1) to v_4) and in the lamellar spacings.

parameter	simulation value				physical value				unit
	r_1)	r_2)	r_3)		r_1)	r_2)	r_3)		$[J/m^2]$
$\gamma_{\alpha\beta}$	0.24	0.2875	0.3		0.12	0.1436	0.15		
$\gamma_{\alpha\ell}$	0.16	0.1125	0.1		0.08	0.0563	0.05		
R	1.5	2.5	3.0		1.5	2.5	3.0		
D	d_1)	d_2)	d_3)		d_1)	d_2)	d_3)	$\cdot 10^{-9}$	$[m^2/s]$
	3	4	5		4.59	6.08	7.6		
∇T	t_1)	t_2)	t_3)	$\cdot 10^{-4}$	t_1)	t_2)	t_3)		
	0.5	1	2		100	200	400		$[K/mm]$
v of ∇T	v_1)	v_2)		$\cdot 10^{-3}$	v_1)	v_2)		$\cdot 10^{-2}$	$[mm/s]$
	2.3	2.8			0.89	1.09			
	v_3)	v_4)			v_3)	v_4)			
	3.4	3.97			1.32	1.54			
λ	60 until 140				$2.334 \cdot 10^{-5}$ until $5.446 \cdot 10^{-5}$				$[m]$

Due to the diffusion, which is multiple times faster in the liquid than in the solid [43], the solid-state diffusion is neglected. Hence, the solid phases do not perform any further phase transformations after they solidified. Because of this assumption, a moving window approach is employed to reduce the computational effort [1,31,44].

As mentioned in [24], tilted growth can occur for certain ratios of the interface energies. The tilt angle θ is defined as the difference between the direction of the imprinted temperature gradient and the solid-solid interfaces. For the studies in this work, the tilt angles depending on certain combinations of the diffusion coefficients, the interface energy ratios, the lamellar spacings, the growth velocities and the slope of the temperature gradients are investigated. The used simulation parameters from [24] are given in Table 1. The values of the systematically varied quantities are collected in Table 2.

2.3. Measurement of the tilt angle

To study the dependence of the tilt angle on the physical parameters and on the process parameters in an automatized manner, an unsupervised measuring technique is required. A computational algorithm to analyze the results from extensive phase-field studies is applied, which is described in the following.

After conducting the simulations, a marching cube algorithm [45] is utilized to determine the solid-solid interfaces with equal order parameters. Then the periodic boundary conditions are exploited to obtain a continuous interface between the solid phases over the whole growth height as depicted in Fig. 2. This is achieved by shifting the solid-solid phase boundaries with amounts of the natural multipliers of λ.

To measure the tilt angle, a rotated coordinate system, denoted by x^*-z^* is considered. Therefore, a linear interpolation of the considered boundary is conducted to determine the local maxima in the direction of x^*. In the next step, the local maxima are evaluated, and a linear least squares fitting procedure is applied. Even in simulations with visually straight interfaces, multiple small maxima are found, which are used for the fitting procedure. After determining the slope in the x^*-z^*-system, the average tilt angle is attained with respect to the original x-z-system.

By constructing a larger microstructure through the shifting of λ, continuous solid-solid interfaces are formed and the number of maxima is increased to ensure a high accuracy of the measured tilt angles. For the calculation of the tilt angle, a minimum number of four local maxima is required.

3. Results and discussion

In the following, the dependences of the tilt angles on the varied parameters are presented and discussed. The tilt angles are measured with the method presented in Section 2.3. In the first part of this section, the utilized automatic analyzing method is
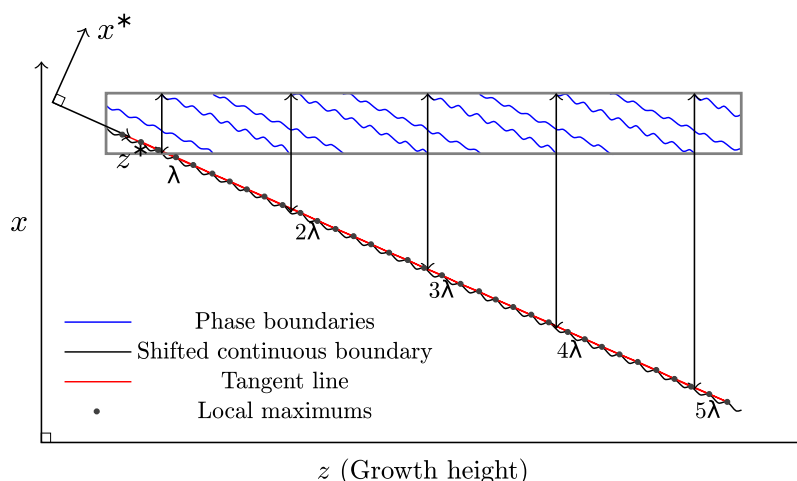

Fig. 2. The shifting of λ and the formation of a continuous phase boundary for calculation of the tilt angle.

validated by remeasuring a selection of results from [24]. In the second part, the ratio of the interface energies R, the diffusion coefficient D, the temperature gradient G and the growth velocity v is systematically varied and their effects on the tilt angle are shown. In the third part, the dimensionless Péclet number is used to combine and compare the results from the different parameters. Based on these results, a fitting approach is derived to predict the tilt angle.

3.1. Validation of the measuring method

To validate the automatic measuring method, the manually obtained tilt angles in [24] are remeasured. In Fig. 3, the original measurement results for the parameters given in [24] for $R = 3$ are plotted over the lamellar spacing λ with green diamonds. The curves of the tilt angle show a global maximum at $\lambda = \lambda_{peak}$. For growth deviations of the lamellar spacing from λ_{peak}, a decrease of the tilt angle is observed. For $\lambda \leqslant \lambda_{peak}$, stationary lamellar growth is observed and, for $\lambda > \lambda_{peak}$, an oscillation of the phase widths occurs, which increases for higher values of the lamellar spacing.

In Fig. 3, the tilt angles over the lamellar spacings from the automatized approach are depicted as blue squares. A good qualitative agreement is found between the results of both methods. For the hand measured results in [24], λ_{peak} is located at $\lambda \approx 89$ with $\theta = 7.14°$, and for the automatized method, the peak occurs at $\lambda \approx 86$, with $\theta = 7.065°$. For $\lambda < \lambda_{peak}$ the maximum deviation between the two measurements is $0.05°$ (1%), whereas the deviations for $\lambda > \lambda_{peak}$ become larger with up to $0.63°$ (10%) at $\lambda = 95$. This can be explained by the error, which is due to the hand measurement of the angle from the oscillating phase widths. The results show the capability of the automatized measuring approach to quantitatively capture the resulting tilt angles from the simulations.

3.2. Systematic variation of the physical parameters and the process parameters

With the validated measuring method, the influences of different parameters on the tilt angle are investigated. Starting from the system presented in [24], simulation studies with independent modifications of the system parameters are conducted. The
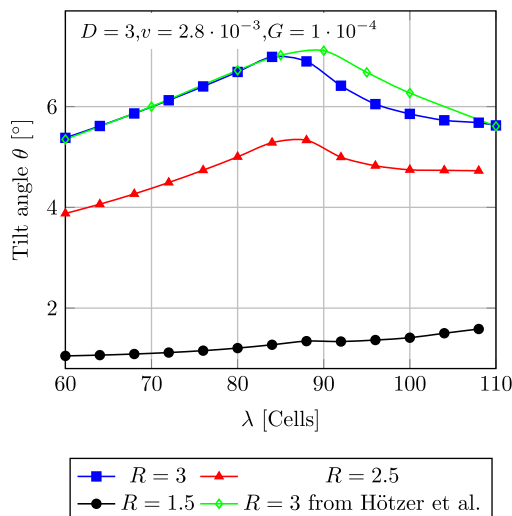

Fig. 3. Variation of the tilt angle over the lamellar spacing for the three different interface energy ratios R. The green diamond line is extracted from [24]. (For interpretation of the references to colour in this figure legend, the reader is referred to the web version of this article.)

domains are systematically increased until one of the phases is overgrown. In the first two simulation studies, the influences of the material specific physical parameters: the interface energy ratios and the diffusion coefficients on tilted growth are investigated. Due to the variation of the process parameters: the temperature gradient and its velocity, the behavior of the tilt angles is studied in the follow-up simulation series. In total, more than 950 simulations are conducted in the studies.

3.2.1. Influence of the interface energy ratio R

Due to the effect of the interface energies on the curvature of the solidification front, the response of the tilt angle is systematically analyzed. As shown in [24], tilting of phases occurs for special ratios of isotropic interface energies.

For the study three different ratios of the interface energies $R = \gamma_{\alpha\beta}/\gamma_{\alpha\ell}$ with $R = 0.24/0.16 = 1.5, R = 0.2875/0.1125 = 2.5$ and $R = 0.3/0.1 = 3$ are considered. In Fig. 3, the results are respectively plotted over the lamellar spacing as black circles, red triangles and blue squares.

The investigated ratios illustrate the influence of the different interface energies on the tilt angle. For larger ratios, the tilt angle increases in agreement with the results in [24]. For ratios larger than 3.0, the triple points become unstable in accordance with Young's equation. All curves show a similar shape with a local maximum λ_{peak} at approximately 85 cells. However, for the ratio 1.5, the local extremum at this point is not a global maximum for the considered lamellar spacings. With an increasing lamellar spacing, the tilt angle for the interface energy ratio $R = 1.5$ increases further until one of the phases is overgrown.

3.2.2. Influence of the diffusion coefficient D

As shown in [23], tilted growth can also occur as a result of concentration fluxes and rejections of the chemical elements from the growing solid phases in the melt. For slow solidification with small Péclet numbers ($Pe = \lambda v/D$), the evolving supersaturation depends on the diffusion in the solid phases. Therefore, the influence of the diffusion coefficients in the melt on the arising tilt angle is analyzed. The resulting angles for the diffusion coefficients $D = 3, 4$ and 5, and the ratio 1.5 of the interface energies are plotted in Fig. 4(a) and the results for a ratio of 2.5 are plotted in Fig. 4(b). The other parameters are chosen the same as in the previous study.

As shown in Fig. 4, an increase of diffusion shifts λ_{peak} to higher lamellar spacings, whereas the amount of the tilt angle is decreased. The shift of λ_{peak} is caused by the higher stable phase widths and the less distinct oscillations for larger diffusion coefficients. The evolving supersaturation of the chemical elements in the melt is less pronounced, resulting in a smaller influence of the mechanism described in [23]. These results indicate that besides the tilt mechanism caused by the ratio of the interface energies, an additional flux dependent mechanism is active.

3.2.3. Influence of the temperature gradient G

Next, the influence of different process conditions on the tilt angles is studied. First, the non-dimensionalized temperature gradients of $5 \cdot 10^{-5}, 10 \cdot 10^{-5}$ and $20 \cdot 10^{-5}$ are used. The resulting tilt angles over the lamellar spacings are depicted in Fig. 5 for a fixed growth velocity of $2.8 \cdot 10^{-3}$, for a ratio of the interface energies, 2.5, and for two different constant diffusion coefficients, 3 and 5.

Although a slight tendency to higher tilt angles can be observed by increasing the temperature gradient, the overall impact is less pronounced than for the previously investigated physical parameters. A similar finding of small influences of the temperature gradient on the tilt angle is found for cellular growth in the work of Akamatsu and Ihle [15], using numerical and experimental studies.
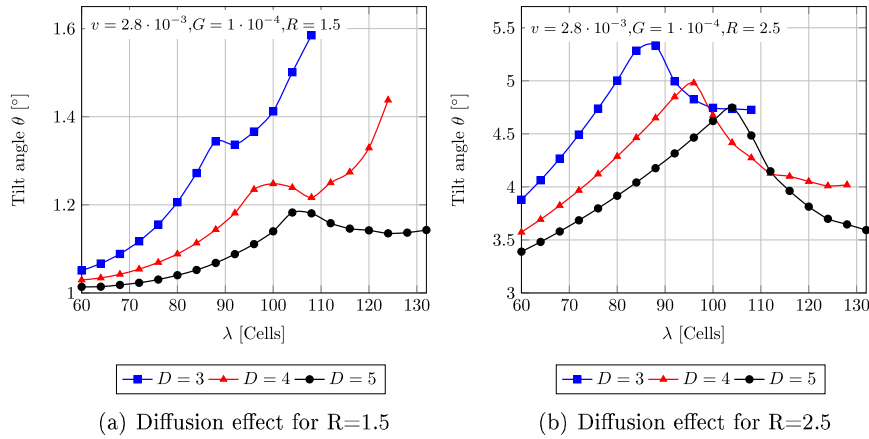
(a) Diffusion effect for R=1.5

(b) Diffusion effect for R=2.5

Fig. 4. Variation of the tilt angle over the lamellar spacing depending on the diffusion coefficients D in the melt for two different interface energy ratios $R = 1.5$ and $R = 2.5$.
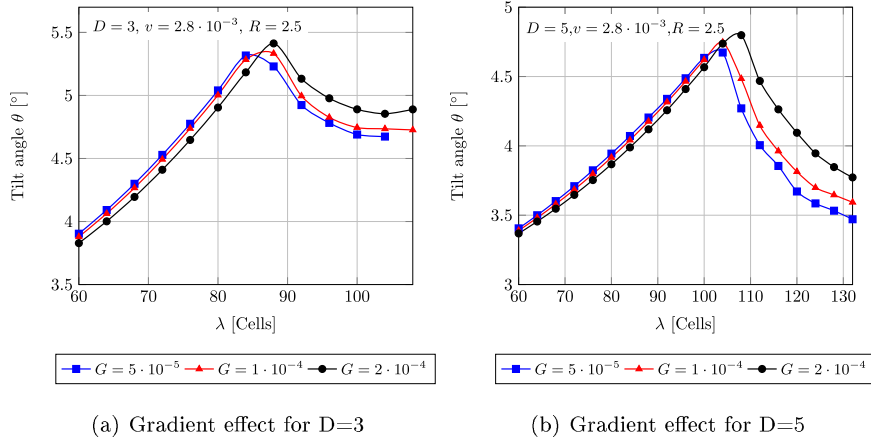

(a) Gradient effect for D=3

(b) Gradient effect for D=5

Fig. 5. Variation of the tilt angle over the lamellar spacing depending on the temperature gradient G for two different diffusion coefficients $D = 3$ and $D = 5$.

For $\lambda > \lambda_{peak}$ the derivations between the curves become larger, due to the more pronounced oscillations of the solid phases, which are not only parallel to the solidification front, but also in the growth direction.

3.2.4. Influence of the growth velocity v

In the following, the influence of the growth velocity on the measured tilt angle is studied. The velocity is varied from $2.3 \cdot 10^{-3}$ to $3.97 \cdot 10^{-3}$, according to the steps presented in Table 2.

The resulting tilt angles are depicted in Fig. 6. For higher velocities, both the lamellar spacing with the maximum angle and the angles at λ_{peak} are smaller. The shifting of λ_{peak} is related to the less pronounced diffusion process for higher velocities. Additionally, the slopes of the curves for the tilt angles at $\lambda < \lambda_{peak}$ are similar for all investigated velocities. With increasing velocity, the tilt angle first increases until a certain value is exceeded. A further increase results in smaller tilt angles at $\lambda < \lambda_{peak}$. This behavior can be explained by the interplay between the two velocity dependent mechanisms of (i) concentration diffusion and (ii) driving force in the direction of the imprinted temperature gradient.

For $\lambda > \lambda_{peak}$, it can be observed that the decrease of the tilt angle is less pronounced for smaller velocities. Accordingly, the peak of the curves is sharper for higher velocities leading to a smaller range of lamellar spacings with high tilt angles. For a further decrease of the velocity with lower diffusion coefficients, an increase of the tilt angles can be observed for $\lambda > \lambda_{peak}$, similar to the results of $R = 1.5$. Resulting from the interplay between the driving force from the undercooling and the concentration flux, the angle at λ_{peak} decreases, in the case of low velocities and high diffusion coefficients, leading to small Péclet numbers.

3.2.5. Overview of the influencing parameters

In the previous studies, it could be shown with extensive phase-field simulations, that the analyzed physical parameters (R, D) and the process conditions (G, v, λ) influence the evolving tilt angles. The effect of the temperature gradient is small compared to the other parameters. A summary of the behavior of λ_{peak} and of the maximum tilt angles at these points, depending on the parameters, is given in Fig. 7.

In [15,18], the dimensionless Péclet number is utilized to characterize the tilt angle dependences. The correlation between the tilt angle and the Péclet number is depicted in Fig. 8. The interface energy ratio $R = 1.5$ is indicated with red diamonds and $R = 2.5$ with blue points. By plotting the tilt angle of the simulation results of sections 3.2.1, 3.2.2, 3.2.3, 3.2.4 with respect to the Péclet number, the shape of the data points prescribes the same characteristics as the tilt angle plotted over λ. Corresponding to $\lambda_{peak}, Pe_{peak}$ is introduced. For an increasing Péclet number, which can be interpreted as a deviation from diffusion controlled growth,

(a) Velocity effect for D=3   (b) Velocity effect for D=5
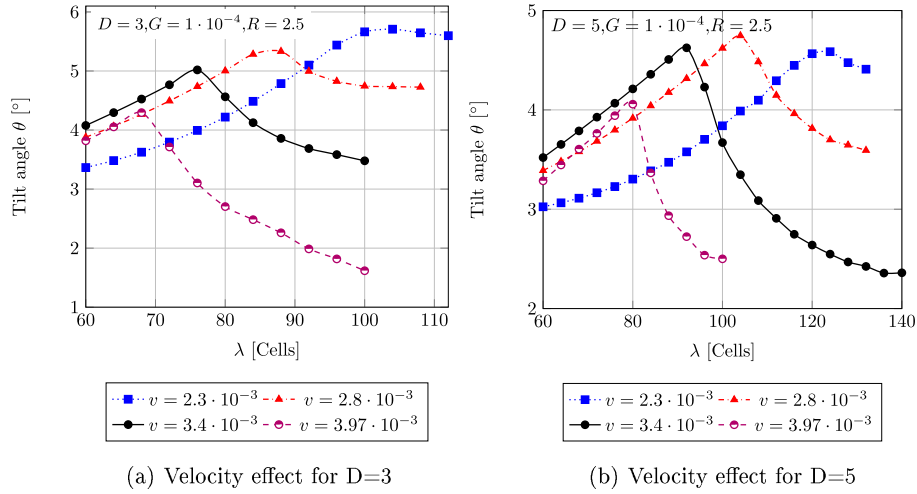
Fig. 6. Variation of the tilt angle over the lamellar spacing depending on the pulling velocity v of the temperature gradient for two different diffusion coefficients $D = 3$ and $D = 5$.
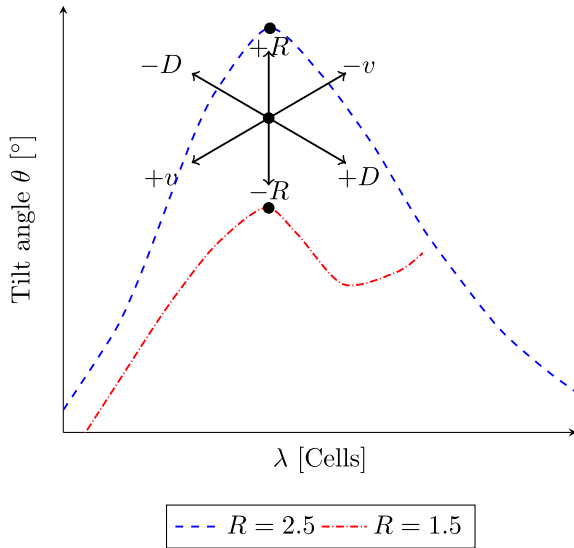

Fig. 7. Schematic illustration of the influence of the physical parameters and the process parameters on the tilt angle of λ_{peak}.

a stronger scattering of the tilt angle is observed. For $Pe > Pe_{peak}$, an additional increase of oscillations occurs in the phase boundaries.

3.3. Fitting of the tilt angle

Due to the lack of a general analytic description of the relationship between the tilt angle, the process parameters and the physical parameters, a fitting approach is introduced to predict the tilt angle.

In Section 3.2.5 two different behaviors in the growth modes are observed: stable lamellar growth ($Pe \leqslant Pe_{peak}$), and oscillation patterns ($Pe > Pe_{peak}$). Different effects on the tilt angle for $Pe > Pe_{peak}$ occur from the interplay between velocity and diffusion. To model these behaviors, a piecewise representation with two different definitions is constructed, minimizing the variance of the tilt angle reported in Fig. 8.

To derive an appropriate fitting, a mapping of the data to a less scattering space is conducted. Depending on Pe_{peak}, two different approaches are applied. For $Pe \leqslant Pe_{peak}$, the Péclet number is mapped onto λPe, and for $Pe > Pe_{peak}$, it is mapped onto $v D^{5/3} Pe^2$.
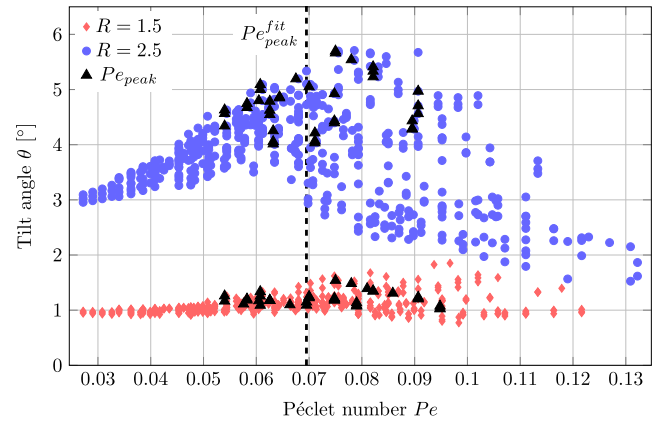

Fig. 8. Tilt angle with respect to the Péclet number (dashed line: $Pe_{peak}^{fit} = 0.0695$).

Before these mappings, the average scattering is determined as 12.4° for $R = 1.5$, with a variance of 0.09, and as 47.03° for $R = 2.5$, with a variance of 1.22. After the mapping process, these values decrease to 8.53° for $R = 1.5$,with a variance of 0.042, and to 29.56° for $R = 2.5$, with a variance of 0.157. By using a cross-validation of the fitting function for the velocities and the diffusivities, the proposed approach performs a convincing applicability with an average error of 7.28% in the investigated parameter range.

To model the tilt angle dependence based on the mapped data, a polynomial fitting approach with modified Péclet numbers is applied, given by the expressions:

$$\theta(D, v, \lambda, R)[°] = \begin{cases} A_1 (\lambda Pe)^2 + B_1 (\lambda Pe) + C_1 & \text{if } Pe \leqslant Pe_{peak}^{fit} \\ A_2 \left(v D^{5/3} Pe^2 \right)^2 + B_2 \left(v D^{5/3} Pe^2 \right) + C_2 & \text{else} \end{cases}$$

(7)

Due to its small impact, the influence of the temperature gradient is neglected in the fit, as discussed in Section 3.2.3.

For the fitting approach in Eq. (7), Pe_{peak}^{fit} is derived as $Pe_{peak}^{fit} = 0.0695$ by systematically minimizing the average error. In Fig. 8, the Péclet number Pe_{peak}^{fit} is shown as a black dashed line. The fitting parameters A_i, B_i and C_i from Eq. (7), are derived by a

Table 3
Interfacial energy ratio dependent fitting function coefficients.

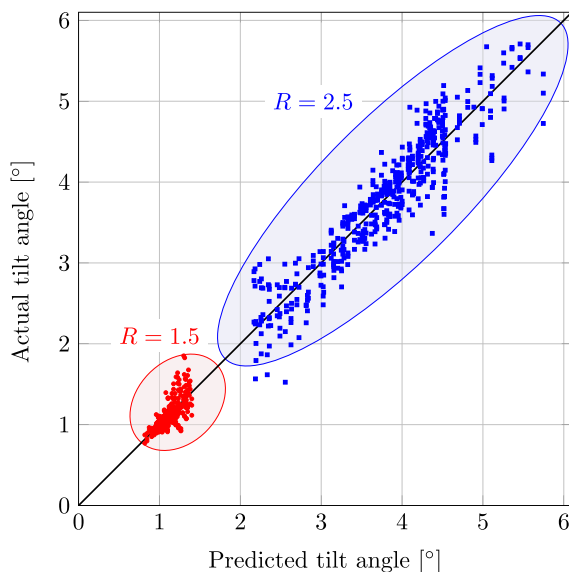|	A	B	C
1	$-0.05006R + 0.07668$	$0.6939R - 1.0133$	$0.95145R - 0.52444$
2	$15712117.267R - 22670209.5675$	$-15945.0451R + 22172.76245$	$5.36291R - 6.529$

Fig. 9. Comparison of measured and predicted tilt angles for two interface energy ratios $R = 1.5$ and $R = 2.5$.

least squares fit and are summarized in Table 3. The parameters are modeled linearly dependent on the interface energy ratios R.

To validate the predicted tilt angles, a comparison with the measured results is plotted in Fig. 9. The results for $R = 1.5$ and $R = 2.5$ are marked in red circles and blue squares, respectively. Referring to the measured angles, the average deviations of the predicted tilt angles are 0.07° (6.1%) for $R = 1.5$ and 0.24° (6.87%) for $R = 2.5$. The maximum deviations are 1.031° (32%) and 0.55° (37.1%) for the two investigated ratios.

To further show the ability of the fitting approach to predict the tilt angle in a quantitatively correct manner, a selection of fitted and measured angles is plotted in Fig. 10. It can be seen that both kind of curves follow the same trends.

4. Conclusion

In this work, the effects of different physical parameters and process parameters on the tilt angle of the solid phases evolving during the directional solidification of idealized ternary eutectic systems with isotropic interface energies are studied. Systematic phase-field studies of the diffusion coefficients, the interface energy ratios, the temperature gradients and the solidification velocities are conducted for different lamellar spacings. To analyze the 950 simulations, an automatized unsupervised measuring method of the tilt angle is introduced. Based on the measurements, a fitting approach is derived to quantitatively predict the evolving tilt angles.

The main conclusions of this work are:

(i) The results indicate that, for a certain lamellar spacing, a high tilt angle is favorable for high interface energy ratios, low velocities and low diffusion coefficients. The behavior of these parameters is schematically illustrated in Fig. 7.
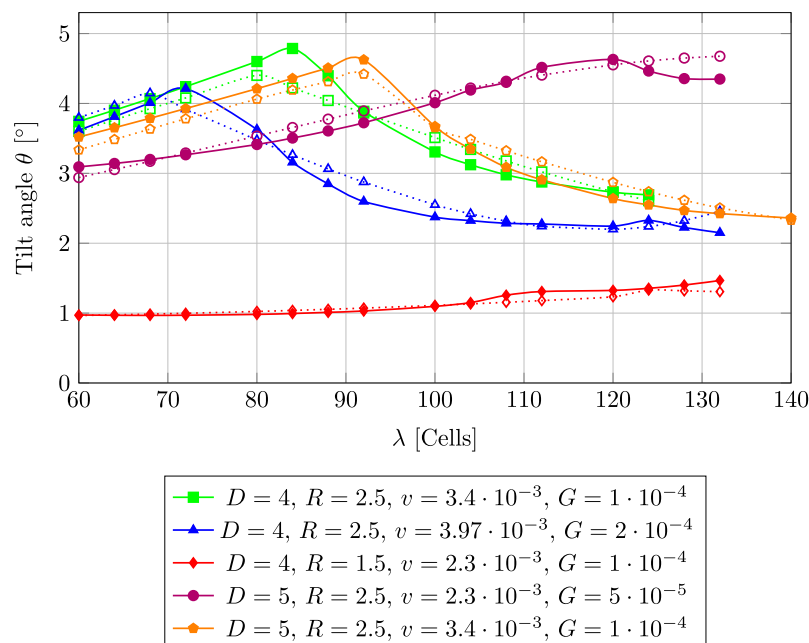

Fig. 10. Comparison of measured (solid curves with filled marks), and predicted (dotted curves with unfilled marks) amounts.

(ii) Compared to these parameters, the influence of the temperature gradient on the tilt angle is less pronounced.

(iii) Due to the complex interplay between the driving force from the undercooling and the concentration flux, it is difficult to draw general conclusions from independent parameter variations. It is found that the evolving tilt angle is a result of both concentration-driven [11] and interface energy-driven mechanisms [24].

(iv) The derived fitting approach predicts the tilt angle in a good quantitative manner.

Due to the wide range of investigated process parameters for various idealized ternary eutectic systems, it can be concluded that the demonstrated trends for tilted growth, are transferable to similar systems.

Acknowledgment

References

[1] J. Hötzer*, M. Kellner*, P. Steinmetz*, B.N. (*equal authors), Applications of the phase-field method for the solidification of microstructures in multi-component systems, J. Indian Inst. Sci. (2016).

[2] W. Kurz, D. Fisher, Fundamentals of solidification, Trans Tech Publications Ltd, Trans Tech House, 4711, Aedermannsdorf, Switzerland, 1986, 244, 1986.

[3] L. Rátkai, G.I. Tóth, L. Környei, T. Pusztai, L. Gránásy, Phase-field modeling of eutectic structures on the nanoscale: the effect of anisotropy, J. Mater. Sci. 52 (2017) 5544–5558.

[4] D. Cooksey, A. Hellawell, The microstructures of ternary eutectic alloys in the systems Cd-Sn-(Pb, In, Ti), Al-Cu-(Mg, Zn, Ag), and Zn-Sn-Pb, J. Inst. Metals 95 (1967) 183–187.

[5] S. Bottin-Rousseau, M. Şerefoğlu, S. Yücetürk, G. Faivre, S. Akamatsu, Stability of three-phase ternary-eutectic growth patterns in thin sample, Acta Mater. 109 (2016) 259–266.

[6] S. Akamatsu, S. Bottin-Rousseau, G. Faivre, Experimental evidence for a zigzag bifurcation in bulk lamellar eutectic growth, Phys. Rev. Lett. 93 (2004) 175701.

[7] M. Plapp, A. Karma, Eutectic colony formation: a phase-field study, Phys. Rev. E 66 (2002) 061608.

[8] A. Lahiri, C. Tiwary, K. Chattopadhyay, A. Choudhury, Eutectic colony formation in systems with interfacial energy anisotropy: a phase field study, Comput. Mater. Sci. 130 (2017) 109–120.

[9] S. Akamatsu, G. Faivre, Traveling waves, two-phase fingers, and eutectic colonies in thin-sample directional solidification of a ternary eutectic alloy, Phys. Rev. E 61 (2000) 3757.

[10] A. Karma, A. Sarkissian, Morphological instabilities of lamellar eutectics, Metall. Mater. Trans. A 27 (1996) 635–656.

[11] M. Apel, B. Boettger, H. Diepers, I. Steinbach, 2D and 3D phase-field simulations of lamella and fibrous eutectic growth, J. Crystal Growth 237 (2002) 154–158.

[12] V. Witusiewicz, U. Hecht, S. Rex, M. Apel, In situ observation of microstructure evolution in low-melting Bi–In–Sn alloys by light microscopy, Acta Materialia 53 (2005) 3663–3669.

[13] M. Plapp, Three-dimensional phase-field simulations of directional solidification, J. Crystal Growth 303 (2007) 49–57.

[14] S. Akamatsu, G. Faivre, Anisotropy-driven dynamics of cellular fronts in directional solidification in thin samples, Phys. Rev. E 58 (1998) 3302.

[15] S. Akamatsu, T. Ihle, Similarity law for the tilt angle of dendrites in directional solidification of non-axially-oriented crystals, Phys. Rev. E 56 (1997) 4479.

[16] S. Akamatsu, M. Plapp, Eutectic and peritectic solidification patterns, Curr. Opin. Solid State Mater. Sci. 20 (2016) 46–54.

[17] K. Kassner, A. Valance, C. Misbah, D. Temkin, New broken-parity state and a transition to anomalous lamellae in eutectic growth, Phys. Rev. E 48 (1993) 1091.

[18] S. Ghosh, A. Choudhury, M. Plapp, S. Bottin-Rousseau, G. Faivre, S. Akamatsu, Interphase anisotropy effects on lamellar eutectics: a numerical study, Phys. Rev. E 91 (2015) 022407.

[19] S. Ghosh, M. Plapp, Influence of interphase anisotropy on lamellar eutectic growth patterns, Trans. Indian Inst. Met. 68 (2015) 1235–1238.

[20] S. Akamatsu, S. Bottin-Rousseau, G. Faivre, S. Ghosh, M. Plapp, Lamellar eutectic growth with anisotropic interphase boundaries, IOP Conference Series: Materials Science and Engineering, vol. 84, IOP Publishing, 2015, p. 012083, 1.

[21] S.G. Kim, W.T. Kim, T. Suzuki, M. Ode, Phase-field modeling of eutectic solidification, J. Crystal Growth 261 (2004) 135–158.

[22] A. Parisi, M. Plapp, Stability of lamellar eutectic growth, Acta Mater. 56 (2008) 1348–1357.

[23] M. Apel, B. Böttger, V. Witusiewicz, U. Hecht, I. Steinbach, Lamellar Pattern Formation during 2D-Directional Solidification of Ternary Eutectic Alloys, Wiley-VCH Verlag GmbH & Co., KGaA, 2005, pp. 271–279.

[24] J. Hötzer, P. Steinmetz, M. Jainta, S. Schulz, M. Kellner, B. Nestler, A. Genau, A. Dennstedt, M. Bauer, H. Köstler, U. R"ude, Phase-field simulations of spiral growth during directional ternary eutectic solidification, Acta Mater. 106 (2016) 249–259.

[25] M. Ginibre, S. Akamatsu, G. Faivre, Experimental determination of the stability diagram of a lamellar eutectic growth front, Phys. Rev. E 56 (1997) 780.

[26] M. Plapp, Unified derivation of phase-field models for alloy solidification from a grand-potential functional, Phys. Rev. E 84 (2011) 031601.

[27] A. Choudhury, B. Nestler, Grand-potential formulation for multicomponent phase transformations combined with thin-interface asymptotics of the double-obstacle potential, Phys. Rev. E 85 (2012) 021602.

[28] J. Hötzer, M. Jainta, P. Steinmetz, B. Nestler, A. Dennstedt, A. Genau, M. Bauer, H. Köstler, U. R"ude, Large scale phase-field simulations of directional ternary eutectic solidification, Acta Mater. 93 (2015) 194–204.

[29] J. Hötzer, O. Tschukin, M. Said, M. Berghoff, M. Jainta, G. Barthelemy, N. Smorchkov, D. Schneider, M. Selzer, B. Nestler, Calibration of a multi-phase field model with quantitative angle measurement, J. Mater. Sci. 51 (2015) 1788–1797.

[30] C. Godenschwager, F. Schornbaum, M. Bauer, H. Köstler, U. Rüde, A framework for hybrid parallel flow simulations with a trillion cells in complex geometries, in: Proceedings of SC13: International Conference for High Performance Computing, Networking, Storage and Analysis, ACM, 2013, p. 35.

[31] M. Bauer, J. Hötzer, M. Jainta, P. Steinmetz, M. Berghoff, F. Schornbaum, C. Godenschwager, H. Köstler, B. Nestler, U. Rüde, Massively parallel phase-field simulations for ternary eutectic directional solidification, in: Proceedings of the International Conference for High Performance Computing, Networking, Storage and Analysis, SC '15, ACM, New York, NY, USA, 2015, pp. 8:1–8:12, http://dx.doi.org/10.1145/2807591.2807662.

[32] J. Hötzer, M. Jainta, M.B. Said, P. Steinmetz, M. Berghoff, B. Nestler, Application of large-scale phase-field simulations in the context of high-performance computing, in: W.E. Nagel, D.H. Kröner, M.M. Resch (Eds.), High Performance Computing in Science and Engineering '15: Transactions of the High Performance Computing Center, Stuttgart (HLRS) 2015, Springer, 2015.

[33] P. Steinmetz, Y. Yabansu, J. Hötzer, M. Jainta, B. Nestler, S. Kalidindi, Analytics for microstructure datasets produced by phase-field simulations, Acta Mater. 103 (2016) 192–203.

[34] P. Steinmetz, M. Kellner, J. Hötzer, A. Dennstedt, B. Nestler, Phase-field study of the pattern formation in al–ag–cu under the influence of the melt concentration, Comput. Mater. Sci. 121 (2016) 6–13.

[35] P. Steinmetz, J. Hötzer, M. Kellner, A. Dennstedt, B. Nestler, Large-scale phase-field simulations of ternary eutectic microstructure evolution, Comput. Mater. Sci. 117 (2016) 205–214.

[36] M. Kellner, I. Sprenger, P. Steinmetz, J. Hötzer, B. Nestler, M. Heilmaier, Phase-field simulation of the microstructure evolution in the eutectic NiAl-34Cr system, Comput. Mater. Sci. 128 (2017) 379–387.

[37] J. Hötzer, P. Steinmetz, M. Kellner, B. Nestler, Large-scale phase-field simulations of directional solidified ternary eutectics using high-performance computing, in: W.E. Nagel, D.H. Kröner, M.M. Resch (Eds.), High Performance Computing in Science and Engineering '16: Transactions of the High Performance Computing Center, Stuttgart (HLRS) 2016, Springer, 2016.

[38] J. Hötzer, M. Jainta, M. Bauer, P. Steinmetz, M. Kellner, H. Köstler, U. Rüde, B. Nestler, High Performance Computing in Science und Engineering – Garching/Munich 2016 (2016), Bayerische Akademie der Wissenschaften, 2016.

[39] B. Nestler, H. Garcke, B. Stinner, Multicomponent alloy solidification: Phase-field modeling and simulations, Phys. Rev. E 71 (2005) 041609.

[40] A. Karma, Phase-field formulation for quantitative modeling of alloy solidification, Phys. Rev. Lett. 87 (2001) 115701.

[41] B. Echebarria, R. Folch, A. Karma, M. Plapp, Quantitative phase-field model of alloy solidification, Phys. Rev. E 70 (2004) 061604.

[42] A. Choudhury, M. Kellner, B. Nestler, A method for coupling the phase-field model based on a grand-potential formalism to thermodynamic databases, Curr. Opin. Solid State Mater. Sci. (2015).

[43] E.L. Cussler, Diffusion: Mass Transfer in Fluid Systems, Cambridge University Press, 2009.

[44] A. Vondrous, M. Selzer, J. Hötzer, B. Nestler, Parallel computing for phase-field models, Int. J. High Perform. Comput. Appl. 28 (2014) 61–72.

[45] W.E. Lorensen, H.E. Cline, Marching cubes: a high resolution 3D surface construction algorithm, ACM Siggraph Computer Graphics, vol. 21, ACM, 1987, pp. 163–169, 4.